Energy conservation law in strong-field photoionization by circularly polarized light

Jonathan Dubois, Camille Lévêque, Jérémie Caillat, Richard Taïeb, Ulf Saalmann, Jan-Michael Rost

Energy conservation law in strong-field photoionization by circularly polarized light

Jonathan Dubois [1,2] Camille Lévêque [1] Jérémie Caillat [1] Richard Taïeb [1] Ulf Saalmann [2] and Jan-Michael Rost [2]

[1] *Sorbonne Université, CNRS, Laboratoire de Chimie Physique–Matière et Rayonnement, LCPMR, 75005 Paris, France*

[2] *Max Planck Institute for the Physics of Complex Systems, Nöthnitzer Straße 38, 01187 Dresden, Germany*

(Received 22 June 2023; accepted 19 December 2023; published 26 January 2024)

We establish an energy conservation law for tunneling electrons driven by a circularly polarized light in a rotationally invariant potential. This conservation law emerges from the adiabaticity of the ionization process when described in the frame rotating with the laser field. It offers a clear picture of nonlinear phenomena observed in strong fields for initial states carrying a magnetic quantum number. It provides unambiguous sets of trajectories to model and interpret cutting-edge experiments using semiclassical approaches.

DOI: 10.1103/PhysRevA.109.013112

I. INTRODUCTION

Tunnel ionization is a fundamental quantum process which plays a key role in advanced probing techniques for measuring the real-time motion of electrons inside atoms and molecules [1–5]. In order to experimentally explore these dynamics on an attosecond timescale, infrared and near-infrared laser pulses are most commonly employed. When the laser intensity is strong enough [6–8], its field combined with the atomic or molecular potential creates a barrier through which a valence electron can tunnel ionize. The subsequent photoelectron dynamics, governed by field-driven rescattering [9], leads to highly nonlinear phenomena such as above-threshold ionization [10] or high-harmonic generation [11]. The latter has been subsequently developed to design "self-probing" spectroscopies with unprecedented time and space resolutions [12,13]. Controlling the conditions under which ionization occurs, modeling the rates and the phase-space configuration of the photoelectron wave packet at the exit are essential theoretical steps for interpreting and decoding the experimental measurements which allow one to retrieve attosecond-resolved information on the probed system.

The essence of tunnel ionization is efficiently captured by adiabatic, quasistatic theories such as Ammosov-Delone-Krainov (ADK) [6,14,15]. However, in this regime, the electron dynamics and the infrared laser period pertain to the same timescale, such that the energy of the electron *during* tunneling is significantly affected by subcycle couplings [16–19], with gains of the order of the electron volt [20–22]. These are nonadiabatic effects [19] and the energy of the electron right after ionization is hard to assess. In atoms, these difficulties are circumvented by neglecting the interaction between the electron and the ion [16–18,20] in the framework of the so-called strong-field approximation [23,24] (SFA). The SFA provides analytic formulas for ionization phenomena and unravels the classical behavior of the electron subjected to strong-laser fields. It is thus an essential ingredient for the design and interpretation of time-resolved experiments using intense laser fields.

While the essentials of strong-field physics can be addressed by considering linearly polarized pulses, circularly polarized (CP) fields valuably offer additional experimental ways of probing ultrafast dynamics in atoms and molecules, including chiral species [25], as demonstrated with the "attoclock" setup [26,27]. In this context, the semiclassical treatment of strong-field ionization has raised passionate debates regarding the time spent by the electron under the potential barrier [28–31]. There, it was established that the electron-ion interaction plays a crucial role and cannot be overlooked in attempts to interpret the phase-space configuration of the electron [30,32,33]. From the modeling perspective, while perturbative approaches are valuable [28], a major bottleneck comes from the complexity of fully taking into account the Coulomb effects and the nonadiabatic ones all at once *during* and *after* tunneling [31,32,34].

In this article, we show that tunnel ionization of electrons by time-dependent CP fields obeys an energy conservation law using analytical developments supported by numerical simulations. In Sec. II, we evidence, with numerical simulations on model atoms, the essential features of the electron energy distribution upon tunneling in CP fields and their dependency with respect to the initial-state magnetic orientation. In Sec. III, we derive a rigorous photoelectron energy conservation law emerging in the rotating frame (RF) by fully taking into account the ion-electron interaction and disentangling nonadiabatic effects occurring on short and long timescales in the laboratory frame (LF). In Sec. IV, we show that the conservation law in the RF translates into the conversion of angular momentum into energy in the LF. We illustrate the relevance of our findings to applied strong-field physics by further analyzing the observable outcomes of the numerical simulations in the light of this conservation law.

II. ENERGY DISTRIBUTIONS UPON TUNNELING

We consider a single active electron in a two-dimensional (2D) atom interacting with a classical electric field in the dipole approximation within the length gauge. The Hamiltonian governing the electron dynamics is

$$H(t) = \frac{\mathbf{p}^2}{2} + V(r) + \mathbf{r}\cdot\mathbf{F}(t), \tag{1}$$

where $\mathbf{r}$ is the electron position (r its distance to the nucleus), $V(r)$ is the ion-electron energy potential, and $\mathbf{p}$ is the momentum operator. Hamiltonian (1) is expressed in the LF, i.e., the frame in which the electrons are detected in experiments. We consider ion-electron energy potentials which are invariant under rotations, which typically corresponds to atomic potentials [35] (and, to some extent, to molecules modeled by a continuous potential such as benzene [36] and buckminsterfullerene [37]). To address the specificities of CP driven dynamics, we performed 2D simulations for He initially in its $1s$ ($m = 0$) state (with ionization potential $I_p = 24.3$ eV), H is initially in its 1s (m = 0) state ($I_p = 13.6$ eV) or Ne initially in either of its $2p_\pm$ ($m = \pm 1$) states ($I_p = 21.6$ eV). We used model potentials with the generic form [35]

$$V(r) = -\frac{1 + b\exp(-r^2)}{\sqrt{r^2 + a^2}}, \tag{2}$$

where the parameters are adapted to each model atom ($a = 0.26$, $b = 0$ for He [38], $a = 1.7$, $b = 9$ for Ne [39], $a = 0.7977$, $b = 0$ for H). Numerically, the initial-state wave function $\psi_0(\mathbf{r})$ and I_p for each model atom were obtained using imaginary-time propagation [40]. The time-dependent CP laser electric field is defined as $\mathbf{F}(t) = -\partial_t \mathbf{A}(t)$, where $\mathbf{A}(t)$ is the associated vector potential,

$$\mathbf{A}(t) = A_0 f(t)[\mathbf{e}_x \cos(\omega t) + \mathbf{e}_y \sin(\omega t)], \tag{3}$$

with $A_0 = F_0/\omega$, ω the laser frequency and F_0 the peak field amplitude leading to a peak intensity $I = 2F_0^2$. We use an infrared pulse of 800 nm wavelength and a 2-cycle $\sin^4$ envelope given as $f(t) = \cos(\pi t/\tau)^4$ for $|t| \leqslant \tau/2$ and zero otherwise, with $\tau = 4\times 2\pi/\omega$. Considering $\mathbf{e}_z$ (orthogonal to the polarization plane) as the quantization axis, a $m = +1$ or $m = -1$ electron is therefore co- or counter-rotating with the laser field, respectively.

The $(\mathbf{r}, \mathbf{p})$ phase-space distributions, right after tunneling and fully taking into account the ion-electron interaction, are obtained using the backpropagation method. This approach, detailed in [22,29], can be summarized in four steps: (i) The wave function $\psi(\mathbf{r}, t)$, starting from the initial state $\psi_0(\mathbf{r})$, is propagated forward quantum mechanically using the time-dependent Schrödinger equation (TDSE),

$$i\partial_t \psi(\mathbf{r}, t) = H(t)\,\psi(\mathbf{r}, t), \tag{4}$$

until one cycle after the end of the laser pulse, i.e., $T = 3\times 2\pi/\omega$. (ii) From $\psi(\mathbf{r}, T)$, we extract the classical phase-space distribution at T, which is then (iii) propagated backward, using Hamilton's equations, until (iv) we match the tunneling condition, corresponding to the vanishing of the longitudinal momentum. These equations are defined from the classical analog of $H(t)$ [Eq. (1)], hereafter referred to as $\mathcal{H}(\mathbf{r}, \mathbf{p}, t)$ (throughout the text, calligraphic letters stand for classical analogs).

TABLE I. Statistical quantities characterizing the energy and angular distributions of the electron after tunneling in the laboratory frame and in the rotating frame (see Fig. 1 and text). In the former, the distribution of $E + I_p$ is fitted by a Gaussian with mean value e and width Δe. In the latter, the distribution of $\widetilde{E} + (I_p + m\omega)$ is fitted by a Gaussian with mean value $\widetilde{e}$ and width $\Delta\widetilde{e}$. The distribution of $\sphericalangle(-\mathbf{r}, \mathbf{F}(t))$ is fitted by a Gaussian with mean value θ and width $\Delta\theta$.

Atom	He $1s$	Ne $2p_-$	Ne $2p_+$
e (eV)	1.642	2.362	0.958
Δe (eV)	2.064	1.839	2.070
$\widetilde{e}$ (eV)	−0.032	0.048	−0.013
$\Delta\widetilde{e}$ (eV)	0.113	0.102	0.120
θ (deg)	0.452	1.331	0.205
$\Delta\theta$ (deg)	6.728	7.561	6.632

Figure 1 displays the reconstructed energy distributions in the He case [Figs. 1(a), red] and in the Ne cases [Figs. 1(c), green ($m = -1$) and blue ($m = +1$)]. Five main features emerge from this figure. First, we clearly see in Fig. 1(c1) that the ionization probability is larger for an initially counter-rotating electron than for a co-rotating one, in agreement with [20,27,41]. Second, Figs. 1(a1) and 1(c1) show that starting from a δ-function at $-I_p$, the energy distribution shifts towards higher energies (by around 1 eV) and gains a width of about 2 eV during the process. This is a clear signature of nonadiabatic effects and was also observed in [22]. Third, Fig. 1(c1) also shows that for oriented initial states, the photoelectron peak shifts towards higher energies roughly twice more, and with a smaller width, for $m = -1$ than for $m = +1$. These three first features are supported by the quantitative data reported in the first two lines of Table I. Fourth, in Figs. 1(a2) and 1(c2), we observe that the obtained comma-shaped electron distributions in the energy-position plane lie close to the potential barrier at the peak amplitude of the laser field (the classically forbidden regions are indicated by gray areas), regardless of its initial energy and its magnetic quantum number. Finally, Figs. 1(a2) and 1(c2) also show that counter-rotating electrons, on average, ionize closer to the origin than co-rotating ones.

We will demonstrate now that these features can be naturally assessed in the frame rotating with the laser field. The fast carrier oscillations at frequency ω present in the LF disappear in the RF, which was the motivation to use it in strong-field physics classically [42,43] or quantum mechanically in the context of high-harmonic generation by bicircularly polarized pulses [44] and ionization by microwaves [45]. In the next section, we will use the RF to analytically identify the effects of subcycle dynamics by comparing observables in the LF and the RF.

III. ROTATING FRAME AND ENERGY CONSERVATION LAW

Switching to the RF is formally achieved by means of the time-dependent matrix $R_\omega(t)$ associated with the rotation of

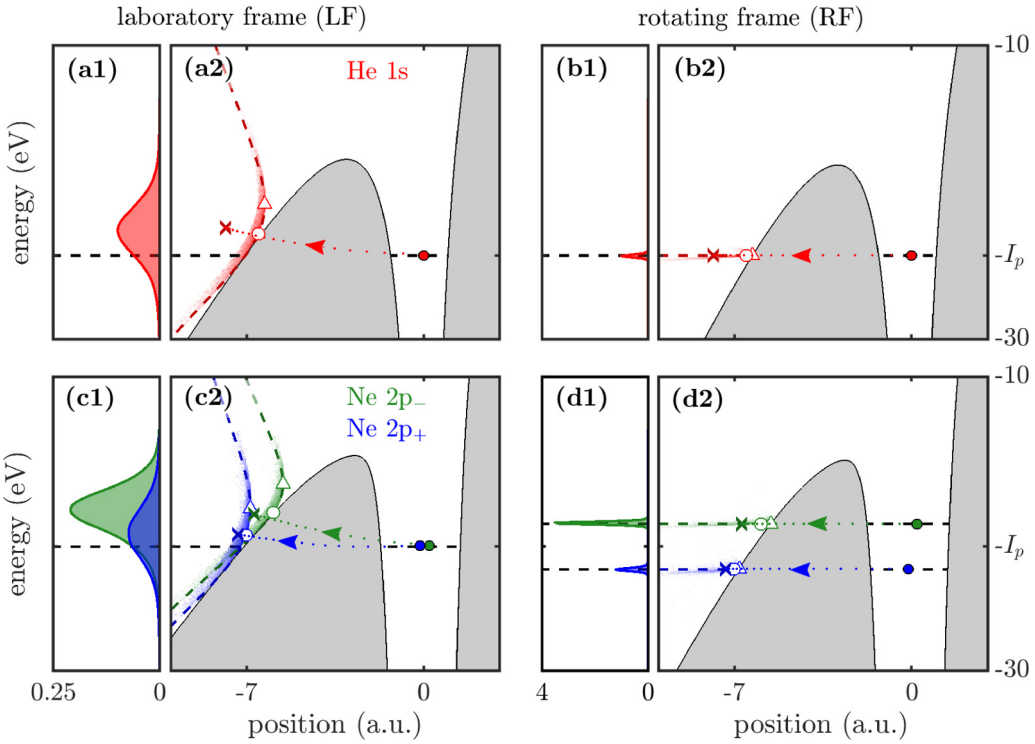

FIG. 1. Phase-space configuration of the electron after ionization obtained from quantum simulations analyzed using the backpropagation method. (a),(c) The distributions in the LF; (b),(d) their counterparts in the RF. Left panels: Distributions of the energy after ionization (normalized with respect to their probability). Right panels: Distributions in energy and in position along the field direction [$\mathbf{F}(t)$ or $\widetilde{\mathbf{F}}(t)$]. The gray regions indicate the classically forbidden region at the peak amplitude of the laser field (i.e., at time $t = 0$). Upper panels: For He, for the initial state $1s$ (red), for $I = 8 \times 10^{14}$ W cm^{-2}. Lower panels: For Ne, for the initial state $2p_-$ (green) and $2p_+$ (blue), for $I = 6 \times 10^{14}$ W cm^{-2}. The open triangles indicate the minimum tunneling distance $r_{\min}$ and associated energies in the LF and in the RF. The dotted lines are complex trajectories from the SFA [23] with initial (colored dots) and final (crosses) conditions (see Appendix B 4). The colored dashed lines and open circles are initial conditions defined by the conservation law (7) (see text).

angle ωt around $\mathbf{e}_z$. The vector potential and the electric field, respectively, become

$$\tilde{\mathbf{A}}(t) = R_\omega(t)\mathbf{A}(t) = A_0 f(t)\mathbf{e}_x, \tag{5a}$$

$$\tilde{\mathbf{F}}(t) = R_\omega(t)\mathbf{F}(t) = -A_0[\dot{f}(t)\mathbf{e}_x + f(t)\omega\mathbf{e}_y]. \tag{5b}$$

Wave functions $\tilde{\psi}$ in the RF are related to ψ in the LF by the unitary transformation [44–46]

$$\widetilde{\psi}(\mathbf{r}, t) = \exp(i\,\omega t\, L_z)\psi(\mathbf{r}, t) \equiv \psi\left(R_\omega^{-1}(t)\mathbf{r}, t\right), \tag{5c}$$

where $L_z = \mathbf{r}\times\mathbf{p}\cdot\mathbf{e}_z$ is the angular momentum component normal to the polarization plane and $\widetilde{\psi}$ is the wave function in the RF. In the RF, the TDSE [Eq. (4)] becomes $i\partial_t\widetilde{\psi} = \widetilde{H}(t)\widetilde{\psi}$, with the Hamiltonian

$$\widetilde{H}(t) = \frac{\mathbf{p}^2}{2} + V(r) - \omega L_z + \mathbf{r}\cdot\widetilde{\mathbf{F}}(t), \tag{6}$$

where the Coriolis term ωL_z results from the time-dependent rotation operator [Eq. (5c)]. Note that the explicit time dependence in the transformation given by Eq. (5c) allows one to assess energy changes, in contrast to time-independent transformations [32]. Due to the rotational invariance of (1) and (6) in the absence of a laser field, the RF Hamiltonian $\widetilde{H}$ shares the same field-free eigenstates as the LF Hamiltonian H, but with shifted eigenenergies due to the Coriolis term. Thus, the ionization potential in the RF is $\widetilde{I}_p = I_p + m\omega$ with $\widetilde{H}(-\infty)\psi_0 = -\widetilde{I}_p\psi_0$; see Appendix A 1. The classical Hamiltonian in the RF is denoted $\widetilde{\mathcal{H}}(\widetilde{\mathbf{r}}, \widetilde{\mathbf{p}}, t)$, where $\widetilde{\mathbf{r}}$ and $\widetilde{\mathbf{p}}$ are the phase-space variables of the electron in the RF. Hamiltonian $\widetilde{\mathcal{H}}$ is obtained either by using the classical analogy of Eq. (6) or, equivalently, by performing the time-dependent canonical transformation $\widetilde{\mathbf{r}} = R_\omega(t)\mathbf{r}$ and $\widetilde{\mathbf{p}} = R_\omega(t)\mathbf{p}$ from $\mathcal{H}$.

In the RF, the time dependence of the electric field is reduced to its envelope $f(t)$, which (i) varies on timescales longer than a laser cycle and (ii) can play the role of an *adiabatic parameter*. Since ionization occurs on timescales much shorter than the pulse duration, standard quasistatic approaches [6,7,14] suggest an electron energy approximately conserved during tunneling. Hence, we expect, at the exit, the RF energy

$$\widetilde{E} = -(I_p + m\omega). \tag{7}$$

This is indeed confirmed by the results displayed in Fig. 2, where we show the distribution of energy gained by the electron *during* ionization in the RF, i.e., $\Delta\widetilde{E} = \widetilde{E} + (I_p + m\omega)$. These distributions (filled curves) are indeed narrow and centered around 0, whereas their LF counterparts (solid lines) are significantly broadened and shifted. More quantitatively, we report in Table I, for all the considered systems, a shift of the photoelectron peak position in the RF ($\widetilde{e}$) of a few tens of meV, i.e., two orders of magnitude lower than in the LF

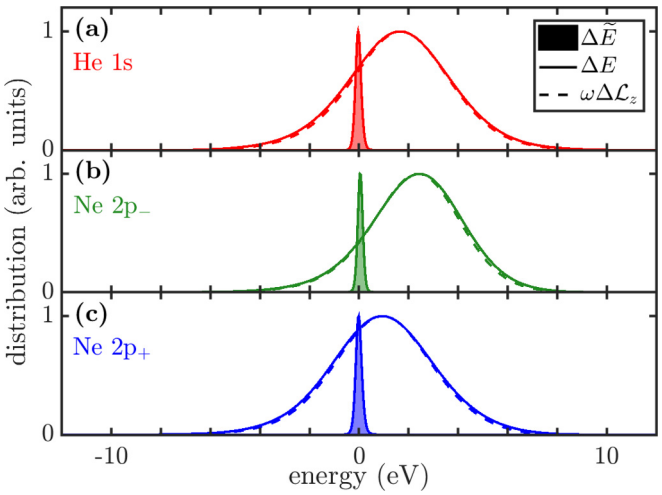

FIG. 2. Distributions of the energy change in the rotating frame $\Delta\widetilde{E} = \widetilde{E} + (I_p + m\omega)$ (filled lines), in the laboratory frame $\Delta E = E + I_p$ (solid lines) and distribution of the inertial energy change $\omega\Delta\mathcal{L}_z = \omega(\mathcal{L}_z - m)$ (dashed lines), corresponding to the distributions of Fig. 1 shifted by their initial energy. All the data were obtained by the backpropagation method and normalized to unity. The Gaussian fit parameters of ΔE and $\Delta\widetilde{E}$ are given in Table I.

(e). The peak width in the RF ($\Delta\widetilde{e}$) is around 100 meV, i.e., one order of magnitude lower than in the LF (Δe). We have checked that the conservation law given in Eq. (7) is robust with respect to field intensities and frequencies. This confirms that tunnel ionization in the RF occurs adiabatically on the energy isosurface,

$$\widetilde{\mathcal{H}}(\widetilde{\mathbf{r}}, \widetilde{\mathbf{p}}, t) = \widetilde{E}, \tag{8}$$

in phase space, where $\widetilde{E}$ results from the m- and ω-dependent electron-ion coupling and laser interactions; see Eq. (7). We have, moreover, found that this conservation law [Eq. (7)] can also be established within the SFA (see Appendix B).

IV. OBSERVABLE SIGNATURES AND APPLICATIONS

In this section, we further analyze the results of the numerical simulations presented in Sec. II and illustrate the relevance of the RF conservation law [Eq. (7)] to deepen our understanding of the mechanisms behind the different outcomes observed in the LF.

First, in the RF, the electron feels the dressed effective potential (see Appendix A 2),

$$\widetilde{V}_{\text{eff}}(\mathbf{r}, t) = V(r) - \frac{\omega^2}{2}(\mathbf{e}_z \times \mathbf{r})^2 + \mathbf{r}\cdot\widetilde{\mathbf{F}}(t), \tag{9a}$$

with kinetic energy

$$\widetilde{K}(\mathbf{r}, \mathbf{p}) = \frac{1}{2}(\mathbf{p} - \omega\,\mathbf{e}_z \times \mathbf{r})^2, \tag{9b}$$

such that $\widetilde{H}(t) = \widetilde{K} + \widetilde{V}_{\text{eff}}(t)$. The classically forbidden regions at the peak of the pulse envelope ($t = 0$, gray areas in Figs. 1(b) and 1(d)] are bounded by $\widetilde{V}_{\text{eff}}(\mathbf{r}, 0)$ and dictate the tunneling dynamics. As observed in Fig. 1(d), both the width and height of the effective barrier through which the electron tunnels in the RF are smaller for a $2p_+$ (smaller $\widetilde{I}_p$) than for a $2p_-$ (larger $\widetilde{I}_p$) initial state. Since tunneling is strongly suppressed with increasing the classically forbidden area, the ionization probability for a counter-rotating electron ($\mathcal{P}_-$) is larger than it is for a co-rotating one ($\mathcal{P}_+$) in strong CP fields in this typical regime, in agreement with the SFA [20], numerical simulations [39], and experimental measurements [27,41]. Furthermore, as the initial energy difference increases for increasing frequencies, the ratio $\mathcal{P}_-/\mathcal{P}_+$ also increases, in agreement with the results of numerical simulations [39].

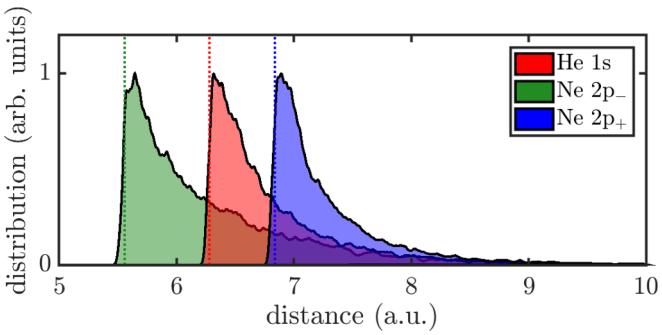

FIG. 3. Distributions of the distance of birth of the electron from the origin obtained by the backpropagation method and normalized to unity corresponding to a projection of the distributions of Fig. 1 on the x axis. The vertical dotted lines are the position of the effective potential barrier r_{min} computed from $\widetilde{V}_{\text{eff}}(-r_{\text{min}}\mathbf{n}_\parallel(0), 0) = -\widetilde{I}_p$ [see Eq. (9a)] with tunneling exit at the peak amplitude of the laser field.

Second, the last two lines of Table I reveal that the electron ionizes mainly along the instantaneous laser electric field direction $\mathbf{n}_\parallel(t) = \widetilde{\mathbf{F}}(t)/|\widetilde{\mathbf{F}}(t)|$ (small θ angles), as predicted from tunneling theories [16–18,20,21,47]. Hence, the position of the electron, which is released into the continuum at t_0, can then be written as $\widetilde{\mathbf{r}} = -r_0\mathbf{n}_\parallel(t_0)$. For each t_0, there is a well-defined *tunneling distance* r_{min}, corresponding to the minimum exit distance [48] that is given by the outermost intersection between the effective potential and the initial energy, i.e., the solution of $\widetilde{V}_{\text{eff}}(-r_{\text{min}}\mathbf{n}_\parallel(t_0), t_0) = -\widetilde{I}_p$ [49]. For each case considered, r_{min} at the peak of the envelope ($t_0 = 0$) is indicated by an open triangle in Fig. 1 and by a vertical dotted line in Fig. 3: it quantitatively matches the minimum exit distance in the distributions obtained by the backpropagation. Furthermore, in the RF, the momentum of the electron "on $\widetilde{V}_{\text{eff}}$" [zero kinetic energy; see Eq. (9b)] is $\widetilde{\mathbf{p}} = \omega\mathbf{e}_z \times \widetilde{\mathbf{r}}$ (see, also, [50]) with $\mathbf{p} = p_{\text{min}}\mathbf{n}_\perp(t_0)$, and therefore $p_{\text{min}} = -\omega r_{\text{min}}$. It is therefore perpendicular to the electric field and nonzero, in agreement with, e.g., Refs. [16–18,20].

Third, because $\mathcal{H}(\mathbf{r}, \mathbf{p}, t) = \widetilde{\mathcal{H}}(\widetilde{\mathbf{r}}, \widetilde{\mathbf{p}}, t) + \omega\mathcal{L}_z$ and according to Eq. (7), the electron angular momentum changes under the barrier are directly converted into energy in the LF. Thus, the conservation law given by Eq. (7) in the RF becomes, in the LF,

$$\Delta E = \omega\,\Delta\mathcal{L}_z, \tag{10}$$

with $\Delta E = E + I_p$ and $\Delta\mathcal{L}_z = \mathcal{L}_z - m$ the energy and angular momentum changes induced by tunneling. Figure 2 shows a comparison between ΔE and $\omega\Delta\mathcal{L}_z$. The perfect agreement between the two curves confirms our findings. Estimations of the angular momentum changes can be further assessed using the tunneling condition established above on the effective

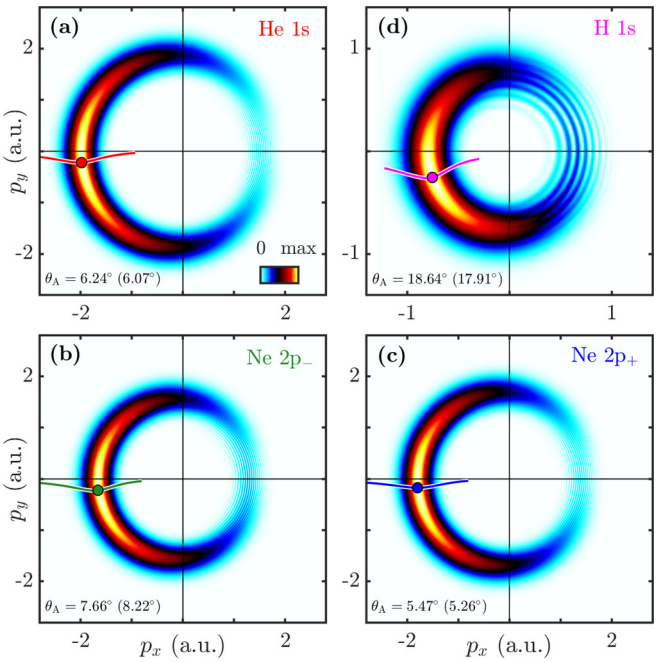

FIG. 4. Photoelectron momentum distributions with (a)–(c) the same parameters as Figs. 1 and 2, and (d) for H with initial state $1s$ and $I = 10^{14}$ W cm^{-2}. In each frame, the colored line is the asymptotic momenta obtained with our fully classical procedure (upon tunneling): The trajectories are obtained from Hamilton's equations with initial conditions given by the conservation law (7) for varying initial transverse momenta. The colored dot indicates the asymptotic momentum for $p_0^{\max}$ and its associated polar angle θ_A is indicated in the bottom-left corner [the value in parentheses is the one obtained from the TDSE (4)].

barrier $\widetilde{V}_{\text{eff}}$, leading to $\mathcal{L}_z = \omega r_{\min}^2$. Accordingly, the energy in the LF upon tunneling for $m = -1$ is larger than for $m = +1$, in fair agreement with the results in Figs. 1 and 2.

Fourth, as we have established that $r_{\min}$ is smaller for $m = -1$ than for $m = +1$, we expect that counter-rotating electrons are subject to stronger Coulomb effects than co-rotating ones. For instance, Coulomb asymmetry [47] can be quantitatively assessed by the attoclock angle θ_A, corresponding to the angle between $-\mathbf{A}(0)$ and the asymptotic momentum for which the photoelectron momentum distribution reaches its maximum value [26,30]. In Fig. 4, we observe that θ_A is indeed larger for the Ne($2p_-$) case [Fig. 4(b)] than for Ne($2p_+$) [Fig. 4(c)], confirming our statements.

Fifth, the conservation law in the RF [Eq. (7)] provides the initial conditions for classical trajectory Monte Carlo methods [26,32,34,51]. It constrains r_0 for a given initial transverse momentum p_0 such that $\widetilde{\mathcal{H}}(-r_0\mathbf{n}_\parallel(t_0), p_0\mathbf{n}_\perp(t_0), t_0) = -\widetilde{I}_p$ with $\mathbf{n}_\perp(t) = \mathbf{e}_z \times \mathbf{n}_\parallel(t)$ (see, also, Appendix A 1 for the determination of the initial conditions with the LF coordinates). To illustrate this, we consider $p_0 \in A_0[-1, 0.5]$ (corresponding to typical values of p_0 [34,51]), which defines a set of initial conditions (colored dashed lines in Fig. 1 [52]), that we integrate with Hamilton's equations. The resulting asymptotic momenta appear as a colored line in each frame of Fig. 4. An estimation of θ_A, indicated in the bottom-left corner of Fig. 4, is deduced from the most probable initial momentum,

TABLE II. Values of positions, momenta, and energy changes for the specific initial conditions considered in the main text. All the r_0 and p_0 (therefore including $r_{\min}$, $p_{\min}$ and $r_0^{\max}$, $p_0^{\max}$) are related through the conservation law $\widetilde{\mathcal{H}}(-r_0\mathbf{n}_\perp(0), p_0\mathbf{n}_\perp(0), 0) = -\widetilde{I}_p$ and $\Delta E = \omega\Delta\mathcal{L}_z$ with $\mathcal{L}_z = -r_0 p_0$, i.e., $\Delta E = -\omega(r_0 p_0 + m)$. In addition, $p_{\min} = -\omega r_{\min}$. The last line is the energy e from the first line of Table I.

Atom	He $1s$	Ne $2p_-$	Ne $2p_+$
$r_{\min}$ (a.u.)	6.281	5.558	6.838
$p_{\min}$ (a.u.)	−0.358	−0.316	−0.389
$\Delta E_{\min}$ (eV)	3.480	4.266	2.569
$r_0^{\max}$ (a.u.)	6.527	5.945	7.016
$p_0^{\max}$ (a.u.)	−0.147	−0.082	−0.215
$\Delta E^{\max}$ (eV)	1.485	2.302	0.787
e (eV)	1.642	2.362	0.958

$p_0^{\max}$, obtained from an extension of the Perelomov-Perentev-Tretenov (PPT) prediction [17,53]. A closed formula for $p_0^{\max}$ is provided in Appendix B 4. Its initial condition is indicated by an open circle in Fig. 1 and its asymptotic momentum by a colored circle in Fig. 4. It shows that the attoclock angle depends sharply on the ionization potential and the magnetic quantum number, as observed in experimental measurements on Kr and Ar [54], even when considering $t_0 = 0$. The comparison with the TDSE calculations for different atomic species and laser parameters clearly supports the qualitative and quantitative predictability character, and the robustness of the results. Furthermore, from $\mathcal{L}_z = -r_0^{\max} p_0^{\max}$ and Eq. (10), we obtain energy gains $\Delta E^{\max}$ of 1.485 eV for He, 2.302 eV for Ne $2p_-$, and 0.787 eV for Ne $2p_+$ (see Table II), in excellent agreement with e in Table I, and Figs. 1 and 2. We observe an excellent agreement between $\Delta E^{\max}$ and e, and a fair agreement between $\Delta E_{\min}$ and e. This mainly comes from the difference between $p_{\min}$ and $p_0^{\max}$, while $r_{\min}$ and $r_0^{\max}$ are roughly the same.

As a final remark, we would like to add that the present scheme of adiabatic time-dependent motion in the RF can be extended to potentials which are not rotationally symmetric, as long as the resulting time dependence of the potential in the RF is slow. Generally speaking, this will be the case for potentials smoothly varying in space, which is the typical case for molecules and more complex chemical species.

V. CONCLUSIONS

To summarize, we have shown that tunnel ionization driven by strong CP laser pulses obeys a classical energy conservation law which translates into intuitive expressions both in the RF [see Eq. (7)] and in the LF [Eq. (10)], and is also accounted for within the SFA (Appendix B). By choosing a proper reference frame and by fully taking into account the ion-electron interaction, we have disentangled nonadiabatic effects occurring on short and long timescales in the laboratory frame. The former is transformed into adiabatic effects where the envelope plays the role of the adiabatic parameter.

In practice, the resultant energy conservation law (7) allows a substantial and accurate reduction of the effective active space when simulating continuum electron dynamics

in strong fields. In addition, it offers a promising avenue for predicting and controlling the phase-space configuration of the electron for more complex systems, such as molecules [55].

This energy conservation law unravels the intrinsic link between the angular momentum of the electron and its energy changes in CP fields. We have used it to characterize nonlinear phenomena from initial states carrying a nonvanishing magnetic quantum number, that can be prepared in diverse ways in experiments [27,41,56], and to resolve the initial conditions in attoclock setups [26,30]. This puts forward the rotating frame coordinates as an alternative "natural" set of coordinates for the attoclock [32].

ACKNOWLEDGMENTS

This research received the financial support of the French National Research Agency through Grant No. ANR-21-CE30-0036-03. J.D. acknowledges Kieran Fraser, Panos Giannakeas, Andrew Hunter, and Gabriel Lando for fruitful discussions.

APPENDIX A: HAMILTONIAN IN THE ROTATING FRAME

1. Ionization potential in the RF

The initial energy in the LF in the absence of a laser field is given by the eigenvalue problem

$$H_0\psi_0(\mathbf{r}) = -I_p\psi_0(\mathbf{r}),\ \ H_0 = \frac{\mathbf{p}^2}{2} + V(r). \tag{A1}$$

Due to the time dependence of the unitary transformation from the LF to the RF, the Hamiltonian in the RF is given by

$$\widetilde{H}_0 = H_0 - \omega L_z. \tag{A2}$$

The initial state is such that $L_z\psi_0 = m\psi_0$, where m is the magnetic quantum number. As a consequence, the eigenvalue problem in the RF becomes

$$\widetilde{H}_0\psi_0 = -(I_p + m\omega)\psi_0,\ \ \widetilde{I}_p = I_p + m\omega, \tag{A3}$$

with ionization potential of the electron in the RF of $\widetilde{I}_p$. It explicitly depends on the magnetic quantum number and the frequency of the circularly polarized laser field.

2. Kinetic and potential energies in the RF

The Hamiltonian in the RF is given by

$$\widetilde{H}(t) = \frac{\mathbf{p}^2}{2} + V(r) - \omega L_z + \mathbf{r}\cdot\widetilde{\mathbf{F}}(t), \tag{A4}$$

where $L_z = \mathbf{r}\times\mathbf{p}\cdot\mathbf{e}_z$ reads also as

$$\widetilde{H}(t) = \widetilde{K} + \widetilde{V}_{\rm eff}(t), \tag{A5a}$$

with kinetic term and effective potentials

$$\widetilde{K} = \frac{1}{2}(\mathbf{p} - \omega\mathbf{e}_z\times\mathbf{r})^2, \tag{A5b}$$

$$\widetilde{V}_{\rm eff}(t) = V(r) - \frac{\omega^2}{2}(\mathbf{e}_z\times\mathbf{r})^2 + \mathbf{r}\cdot\widetilde{\mathbf{F}}(t), \tag{A5c}$$

respectively.

3. Initial conditions in the laboratory frame using the conservation law (7)

Figure 4 shows the photoelectron momentum distributions obtained from the two-dimensional TDSE. Below, we show the detailed derivation to obtain the initial conditions from the conservation law (7). At the tunnel exit at ionization time t_0, we assume that the position is along the laser electric field direction and that the longitudinal momentum vanishes,

$$\mathbf{r}_0 = -r_0\,\mathbf{n}_\parallel(0),\ \ \mathbf{p}_0 = p_0\,\mathbf{n}_\perp(0), \tag{A6a}$$

with

$$\mathbf{n}_\parallel(t_0) = \frac{\mathbf{F}(t_0)}{|\mathbf{F}(t_0)|}, \tag{A6b}$$

$$\mathbf{n}_\perp(t_0) = \mathbf{e}_x[-\mathbf{n}_\parallel(t_0)\cdot\mathbf{e}_y] + \mathbf{e}_y[\mathbf{n}_\parallel(t_0)\cdot\mathbf{e}_x]. \tag{A6c}$$

The unitary vectors are defined such that $\mathbf{n}_\parallel(t_0)\times\mathbf{n}_\perp(t_0)=1$. The angular momentum at the tunnel exit is given by $\mathcal{L}_z = -r_0p_0$. The distance r_0 and momentum p_0 are unknowns. We now use the conservation law [see Eq. (7)], i.e., $\widetilde{H}(\mathbf{r}_0, \mathbf{p}_0, 0) = -\widetilde{I}_p$, that is valid after tunnel ionization, that explicitly reads as

$$-(I_p + m\omega) = \frac{\mathbf{p}_0^2}{2} + V(r_0) - \omega\mathbf{r}_0\times\mathbf{p}_0\cdot\mathbf{e}_z + \mathbf{r}_0\cdot\mathbf{F}(t_0). \tag{A7}$$

We substitute the tunneling assumptions [Eq. (A6a)] and obtain

$$-(I_p + m\omega) = \frac{p_0^2}{2} + V(r_0) + \omega r_0p_0 - r_0|\mathbf{F}(t_0)|. \tag{A8}$$

This equation imposes one constraint on the phase-space configuration of the electron after tunnel exit, and therefore r_0 is fixed by p_0 such that $r_0 = r_0(p_0)$. The dashed lines in Fig. 1 are the resulting initial positions and energies displayed at $t_0 = 0$ (peak amplitude of the laser electric field) for varying p_0. The solid lines in Fig. 4 are the asymptotic momenta of the trajectories obtained from Hamilton's equations with those initial conditions.

APPENDIX B: GREEN FUNCTION IN THE LABORATORY FRAME AND IN THE ROTATING FRAME

1. Strong-field approximation

We show how the classical conservation law emerges naturally from quantum mechanics within the commonly used SFA approach [23]. We start in the LF from the Hamiltonian (1). Within SFA, one uses an ansatz for the electronic wave function as the sum of the initial bound state ψ_0 and an ionized wave packet φ, i.e.,

$$\psi(\mathbf{r}, t) = \exp(iI_pt)\psi_0(\mathbf{r}) + \varphi(\mathbf{r}, t). \tag{B1}$$

After substituting this ansatz in the TDSE and using the SFA assumptions, we obtain

$$\left[i\,\partial_t - \frac{\mathbf{p}^2}{2} - \mathbf{r}\cdot\mathbf{F}(t)\right]\varphi(\mathbf{r}, t) = s(\mathbf{r}, t), \tag{B2}$$

where the ion-electron interaction on the ionizing wave packet is neglected [23], with source term

$$s(\mathbf{r}, t) = [\mathbf{r}\cdot\mathbf{F}(t)]\,\exp(iI_pt)\,\psi_0(\mathbf{r}). \tag{B3}$$

Equation (B2) can be solved within the Green function formalism, for which we obtain the dynamics of the ionizing wave packet governed by

$$\varphi(\mathbf{r},t)=\int_{-\infty}^{t}dt'\int d\mathbf{r}'\,G(\mathbf{r},t;\mathbf{r}',t')\,s(\mathbf{r}',t'). \tag{B4}$$

Notice that the SFA equations (B4) can be equivalently written in the length gauge or velocity gauge, in the position representation or momentum representation. The Green function $G(\mathbf{r},t;\mathbf{r}',t')$ can be exactly expressed in terms of the classical action $\mathcal{S}(\mathbf{r},t;\mathbf{r}',t')$ solution of the Hamilton-Jacobi equation since $\mathcal{H}$ is linear in position for $V=0$ [57],

$$G(\mathbf{r},t;\mathbf{r}',t')=-i\Theta(t-t')\left[\det\left(\frac{1}{2i\pi}\frac{\partial^2\mathcal{S}}{\partial\mathbf{r}\partial\mathbf{r}'}\right)\right]^{1/2}\times\exp[i\mathcal{S}(\mathbf{r},t;\mathbf{r}',t')], \tag{B5}$$

with Θ the Heaviside step function and $\mathcal{S}$ the classical action of the electron explicitly given by

$$\mathcal{S}(\mathbf{r},t;\mathbf{r}',t')=\frac{\left[\mathbf{r}-\mathbf{r}'-\int_{t'}^{t}\mathbf{A}(t'')\,dt''\right]^2}{2(t-t')}+\mathbf{r}\cdot\mathbf{A}(t)-\mathbf{r}'\cdot\mathbf{A}(t')-\frac{1}{2}\int_{t'}^{t}\mathbf{A}(t'')^2\,dt''. \tag{B6}$$

2. Strong-field approximation in the RF

In the RF, the dynamics of φ is obtained by performing the transformation [Eq. (5c)]. We obtain

$$\widetilde{\varphi}(\mathbf{r},t)=\int_{-\infty}^{t}dt'\int d\mathbf{r}'\,\widetilde{G}(\mathbf{r},t;\mathbf{r}',t')\widetilde{s}(\mathbf{r}',t'), \tag{B7}$$

with the source term $\widetilde{s}(R_\omega(t)\mathbf{r},t)=s(\mathbf{r},t)$. There, the initial state accumulates a time-dependent phase, i.e., $\psi_0(R_\omega^{-1}(t)\mathbf{r})=\exp(im\omega t)\psi_0(\mathbf{r})$. Hence the source term becomes

$$\widetilde{s}(\mathbf{r},t)=[\mathbf{r}\cdot\widetilde{\mathbf{F}}(t)]\,\exp(i\widetilde{I}_p t)\,\psi_0(\mathbf{r}), \tag{B8}$$

with $\widetilde{I}_p=I_p+m\omega$. The Green function and the classical action become

$$\widetilde{G}(\mathbf{r},t;\mathbf{r}',t')=G\big(R_\omega^{-1}(t)\mathbf{r},t;R_\omega^{-1}(t')\mathbf{r}',t'\big), \tag{B9}$$

$$\widetilde{\mathcal{S}}(\mathbf{r},t;\mathbf{r}',t')=\mathcal{S}\big(R_\omega^{-1}(t)\mathbf{r},t;R_\omega^{-1}(t')\mathbf{r}',t'\big), \tag{B10}$$

with

$$R_\omega(t)=\begin{pmatrix}\cos(\omega t) & \sin(\omega t) & 0\\ -\sin(\omega t) & \cos(\omega t) & 0\\ 0 & 0 & 1\end{pmatrix}, \tag{B11}$$

and therefore [using $R_\omega(t)R_\omega^{-1}(t')=R_\omega(t-t')$]

$$\widetilde{\mathcal{S}}(\mathbf{r},t;\mathbf{r}',t')=\frac{\left[\mathbf{r}-R_\omega(t-t')\mathbf{r}'-R_\omega(t)\int_{t'}^{t}\mathbf{A}(t'')\,dt''\right]^2}{2(t-t')}+\mathbf{r}\cdot\widetilde{\mathbf{A}}(t)-\mathbf{r}'\cdot\widetilde{\mathbf{A}}(t')-\frac{1}{2}\int_{t'}^{t}\widetilde{\mathbf{A}}(t'')^2\,dt'', \tag{B12}$$

where $\widetilde{\mathbf{A}}(t)=R_\omega(t)\mathbf{A}(t)$. Note that we have numerically verified that Eq. (B7) [or, equivalently, Eq. (B4)] reproduces, with great fidelity, the ionization probabilities of Refs. [20] and [39].

3. Constant laser envelope

On short timescales, around the peak amplitude of the laser field, the pulse envelope is $f(t)=1$, and the vector potential and electric field of the laser in the LF are

$$\mathbf{A}(t)=A_0[\mathbf{e}_x\cos(\omega t)+\mathbf{e}_y\sin(\omega t)], \tag{B13}$$

$$\mathbf{F}(t)=F_0[\mathbf{e}_x\sin(\omega t)-\mathbf{e}_y\cos(\omega t)], \tag{B14}$$

and therefore they are constant in the RF,

$$\widetilde{\mathbf{A}}=R_\omega(t)\mathbf{A}(t)=A_0\mathbf{e}_x, \tag{B15}$$

$$\widetilde{\mathbf{F}}=R_\omega(t)\mathbf{F}(t)=-F_0\mathbf{e}_y. \tag{B16}$$

In addition,

$$\int_{t'}^{t}\mathbf{A}(t'')dt''=\frac{1}{\omega^2}[\mathbf{F}(t)-\mathbf{F}(t')]. \tag{B17}$$

Therefore,

$$R_\omega(t)\int_{t'}^{t}\mathbf{A}(t'')dt''=\frac{1}{\omega^2}[\mathbb{I}-R_\omega(t-t')]\widetilde{\mathbf{F}}, \tag{B18}$$

where $\mathbb{I}$ is the identity. Finally, the classical action in the RF for a circularly polarized pulse with a constant envelope is given by

$$\widetilde{\mathcal{S}}(\mathbf{r},t;\mathbf{r}',t')=\frac{\left[\left(\mathbf{r}-\frac{\widetilde{\mathbf{F}}}{\omega^2}\right)-R_\omega(t-t')\left(\mathbf{r}'-\frac{\widetilde{\mathbf{F}}}{\omega^2}\right)\right]^2}{2(t-t')}+(\mathbf{r}-\mathbf{r}')\cdot\widetilde{\mathbf{A}}-\frac{\widetilde{\mathbf{A}}^2}{2}(t-t'). \tag{B19}$$

The classical action, and therefore the Green function, are invariant under time translation, i.e., $\widetilde{G}(\mathbf{r},t;\mathbf{r}',t')=\widetilde{G}(\mathbf{r},t-t';\mathbf{r}',0)$, regardless of the interaction potential. This clearly indicates that the energy of the ionizing wave packet is conserved during tunnel ionization. The time integral in Eq. (B7) can be substituted by the time-independent Green function $\widetilde{G}(\mathbf{r},\mathbf{r}';-\widetilde{I}_p)$ propagating the electron from $\mathbf{r}'$ to $\mathbf{r}$ on a constant energy level $-\widetilde{I}_p=-(I_p+m\omega)$ and therefore validates the established conservation law (7).

4. Most probable transverse momentum and tunneling trajectory

Equation (B4) can be solved using the saddle-point approximation on the phase of the integrand as described in Refs. [17,23]. From the saddle-point approximation, we get a tunneling rate for the initial transverse momentum p_0, an ionization time t_0, and ϕ. From this rate is deduced that the most probable trajectory ionizes at time $t_0=0$, with a transverse momentum

$$p_0^{\max}=A_0\left[1-\left(1+\frac{m\omega}{2I_p}\right)\frac{\sinh\phi}{\phi}\right], \tag{B20}$$

where ϕ is related to the laser parameters through

$$\gamma^2 = \frac{\sinh(2\phi)}{\phi} - \left(\frac{\sinh\phi}{\phi}\right)^2 - 1 + \frac{m\omega}{I_p}\left[1 - \left(\frac{\sinh\phi}{\phi}\right)^2\right], \tag{B21}$$

and Keldysh parameter $\gamma = \omega\sqrt{2I_p}/F$. It corresponds to an extension of the PPT results [17] for m other than zero. The most probable distance, momentum, and associated energy changes obtained from the conservation law are reported in Table II. The SFA trajectories shown in Fig. 1 of the main text are obtained from the classical action integrated from time $\omega t' = i\phi$ to time $t = 0$ along the imaginary axis of times with position

$$\text{Re}\,\mathbf{r}(t) = -m\frac{\mathbf{e}_z \times [\mathbf{p} - \mathbf{A}(t) + \mathbf{A}(t')]}{\mathbf{e}_z \times [\mathbf{p} - \mathbf{A}(t) + \mathbf{A}(t')]^2} + [\mathbf{p} - \mathbf{A}(t)](t - t') + \int_{t'}^{t} \mathbf{A}(t'')dt'', \tag{B22}$$

and energy

$$E(t) = \frac{\mathbf{p}^2}{2} + \mathbf{r}\cdot\mathbf{F}(t), \tag{B23}$$

with $\mathbf{p} = p_0^{\max}\mathbf{n}_\perp(0)$ the most probable momentum at the tunnel exit.

[1] M. Meckel, D. Comtois, D. Zeidler, A. Staudte, D. Pavičić, H. C. Bandulet, H. Pépin, J. C. Kieffer, R. Dörner, D. M. Villeneuve, and P. B. Corkum, Science **320**, 1478 (2008).

[2] P. B. Corkum, Phys. Today **64**, 36 (2011).

[3] N. G. Kling, K. J. Betsch, M. Zohrabi, S. Zeng, F. Anis, U. Ablikim, B. Jochim, Z. Wang, M. Kübel, M. F. Kling, K. D. Carnes, B. D. Esry, and I. Ben-Itzhak, Phys. Rev. Lett. **111**, 163004 (2013).

[4] L.-Y. Peng, W.-C. Jiang, J.-W. Geng, W.-H. Xiong, and Q. Gong, Phys. Rep. **575**, 1 (2015).

[5] C. D. Lin, A.-T. Le, C. Jin, and H. Wei, J. Phys. B: At., Mol. Opt. Phys. **51**, 104001 (2018).

[6] L. V. Keldysh, Sov. Phys. JETP **20**, 1307 (1965).

[7] B. M. Smirnov and M. I. Chibisov, Sov. Phys. JETP **22**, 585 (1966).

[8] H. R. Reiss, Phys. Rev. A **22**, 1786 (1980).

[9] P. B. Corkum, Phys. Rev. Lett. **71**, 1994 (1993).

[10] G. G. Paulus, W. Becker, W. Nicklich, and H. Walther, J. Phys. B: At. Mol. Opt. Phys. **27**, L703 (1994).

[11] A. L'Huillier and P. Balcou, Phys. Rev. Lett. **70**, 774 (1993).

[12] C. D. Lin, A.-T. Le, Z. Chen, T. Morishita, and R. Lucchese, J. Phys. B: At. Mol. Opt. Phys. **43**, 122001 (2010).

[13] S. Haessler, J. Caillat, and P. Salières, J. Phys. B: At. Mol. Opt. Phys. **44**, 203001 (2011).

[14] M. V. Ammosov, N. B. Delone, and V. P. Krainov, Sov. Phys. JETP **64**, 1191 (1986).

[15] L. Arissian, C. Smeenk, F. Turner, C. Trallero, A. V. Sokolov, D. M. Villeneuve, A. Staudte, and P. B. Corkum, Phys. Rev. Lett. **105**, 133002 (2010).

[16] A. M. Perelomov, V. S. Popov, and M. V. Terent'ev, Sov. Phys. JETP **23**, 924 (1966).

[17] A. M. Perelomov, V. S. Popov, and M. V. Terent'ev, Sov. Phys. JETP **24**, 207 (1967).

[18] A. M. Perelomov and V. S. Popov, Sov. Phys. JETP **25**, 336 (1967).

[19] R. Boge, C. Cirelli, A. S. Landsman, S. Heuser, A. Ludwig, J. Maurer, M. Weger, L. Gallmann, and U. Keller, Phys. Rev. Lett. **111**, 103003 (2013).

[20] I. Barth and O. Smirnova, Phys. Rev. A **84**, 063415 (2011).

[21] M. Klaiber, K. Z. Hatsagortsyan, and C. H. Keitel, Phys. Rev. Lett. **114**, 083001 (2015).

[22] H. Ni, U. Saalmann, and J.-M. Rost, Phys. Rev. A **97**, 013426 (2018).

[23] M. Lewenstein, P. Balcou, M. Y. Ivanov, A. L'Huillier, and P. B. Corkum, Phys. Rev. A **49**, 2117 (1994).

[24] K. Amini, J. Biegert, F. Calegari, A. Chacón, M. F. Ciappina, A. Dauphin, D. K. Efimov, C. F. de Morisson Faria, K. Giergiel, P. Gniewek, A. S. Landsman, M. Lesiuk, M. Mandrysz, A. S. Maxwell, R. Moszyński, L. Ortmann, J. A. Pérez-Hernández, A. Picón, E. Pisanty, J. Prauzner-Bechcicki *et al.*, Rep. Prog. Phys. **82**, 116001 (2019).

[25] S. Beaulieu, A. Comby, A. Clergerie, J. Caillat, D. Descamps, N. Dudovich, B. Fabre, R. Géneaux, F. Légaré, S. Petit, B. Pons, G. Porat, T. Ruchon, R. Taïeb, V. Blanchet, and Y. Mairesse, Science **358**, 1288 (2017).

[26] P. Eckle, A. N. Pfeiffer, C. Cirelli, A. Staudte, R. Dörner, H. G. Muller, M. Büttiker, and U. Keller, Science **322**, 1525 (2008).

[27] S. Eckart, M. Kunitski, M. Richter, A. Hartung, J. Rist, F. Trinter, K. Fehre, N. Schlott, K. Henrichs, L. P. H. Schmidt, T. Jahnke, M. Schöffler, K. Liu, I. Barth, J. Kaushal, F. Morales, M. Ivanov, O. Smirnova, and R. Dörner, Nat. Phys. **14**, 701 (2018).

[28] L. Torlina, F. Morales, J. Kaushal, I. Ivanov, A. Kheifets, A. Zielinski, A. Scrinzi, H. G. Muller, S. Sukiasyan, M. Ivanov, and O. Smirnova, Nat. Phys. **11**, 503 (2015).

[29] H. Ni, U. Saalmann, and J.-M. Rost, Phys. Rev. Lett. **117**, 023002 (2016).

[30] U. S. Sainadh, H. Xu, X. Wang, A. Atia-Tul-Noor, W. C. Wallace, N. Douguet, A. Bray, I. Ivanov, K. Bartschat, A. Kheifets, R. T. Sang, and I. V. Litvinyuk, Nature (London) **568**, 75 (2019).

[31] C. Hofmann, A. Bray, W. Koch, H. Ni, and N. I. Shvetsov-Shilovski, Eur. Phys. J. D **75**, 208 (2021).

[32] A. N. Pfeiffer, C. Cirelli, M. Smolarski, D. Dimitrovski, M. Abu-samha, L. B. Madsen, and U. Keller, Nat. Phys. **8**, 76 (2012).

[33] J. Kaushal and O. Smirnova, J. Phys. B: At., Mol. Opt. Phys. **51**, 174002 (2018).

[34] C. Hofmann, A. S. Landsman, A. Zielinski, C. Cirelli, T. Zimmermann, A. Scrinzi, and U. Keller, Phys. Rev. A **90**, 043406 (2014).

[35] X. M. Tong and C. D. Lin, J. Phys. B: At. Mol. Opt. Phys. **38**, 2593 (2005).

[36] X. Xie, A. Scrinzi, M. Wickenhauser, A. Baltuška, I. Barth, and M. Kitzler, Phys. Rev. Lett. **101**, 033901 (2008).
[37] I. V. Hertel, T. Laarmann, and C. P. Schulz, Ad. At. Mol. Opt. Phys. **50**, 219 (2005).
[38] F. Mauger, A. D. Bandrauk, A. Kamor, T. Uzer, and C. Chandre, J. Phys. B: At. Mol. Opt. Phys. **47**, 041001 (2014).
[39] I. Barth and M. Lein, J. Phys. B: At. Mol. Opt. Phys. **47**, 204016 (2014).
[40] A. D. Bandrauk, E. Dehghanian, and H. Lu, Chem. Phys. Lett. **419**, 346 (2006).
[41] T. Herath, L. Yan, S. K. Lee, and W. Li, Phys. Rev. Lett. **109**, 043004 (2012).
[42] F. Mauger, C. Chandre, and T. Uzer, Phys. Rev. Lett. **105**, 083002 (2010).
[43] A. Kamor, F. Mauger, C. Chandre, and T. Uzer, Phys. Rev. Lett. **110**, 253002 (2013).
[44] D. M. Reich and L. B. Madsen, Phys. Rev. A **93**, 043411 (2016).
[45] A. Buchleitner, D. Delande, and J. Zakrzewski, Phys. Rep. **368**, 409 (2002).
[46] F. Bunkin and A. Prokhorov, Sov. Phys. JETP **19**, 739 (1964).
[47] S. P. Goreslavski, G. G. Paulus, S. V. Popruzhenko, and N. I. Shvetsov-Shilovski, Phys. Rev. Lett. **93**, 233002 (2004).
[48] Note that approaches such as the one we use (including standard ones [34]) provide a well-defined time (i.e., an *instant*) at which the electron exits the tunnel. This is not to be mixed with the notion of tunneling time (i.e., a *duration*), which continuously stimulates a wealth of experimental and theoretical studies, but is outside the scope of the present work [31,58].
[49] At the tunnel exit, the potential is dominantly Coulombic for atoms, i.e., $V(|\widetilde{\mathbf{r}}|) \approx -|\widetilde{\mathbf{r}}|^{-1}$, and hence r_0 barely depends on the system-specific characteristics of the potential.
[50] J. Dubois, C. Chandre, and T. Uzer, Phys. Rev. E **102**, 032218 (2020).
[51] J. Dubois, S. A. Berman, C. Chandre, and T. Uzer, Phys. Rev. A **99**, 053405 (2019).
[52] Considering wider (narrower) ranges elongates (shortens) the lines in Fig. 4 and does not affect the outcome.
[53] Empirically, we find that considering the largest angular deviation within the set of asymptotic momenta also provides a good estimation of the attoclock angle.
[54] N. Camus, E. Yakaboylu, L. Fechner, M. Klaiber, M. Laux, Y. Mi, K. Z. Hatsagortsyan, T. Pfeifer, C. H. Keitel, and R. Moshammer, Phys. Rev. Lett. **119**, 023201 (2017).
[55] E. Bloch, S. Larroque, S. Rozen, S. Beaulieu, A. Comby, S. Beauvarlet, D. Descamps, B. Fabre, S. Petit, R. Taïeb, A. J. Uzan, V. Blanchet, N. Dudovich, B. Pons, and Y. Mairesse, Phys. Rev. X **11**, 041056 (2021).
[56] D. Dowek and J. Houver, Nucl. Instrum. Methods Phys. Res., Sec. B **124**, 232 (1997).
[57] R. G. Littlejohn, J. Stat. Phys. **68**, 7 (1992).
[58] U. S. Sainadh, R. T. Sang, and I. V. Litvinyuk, J. Phys.: Photon. **2**, 042002 (2020).